The Astrophysical Journal, 722:1577–1588, 2010 October 20 doi:10.1088/0004-637X/722/2/1577

MANIFESTATIONS OF ENERGETIC ELECTRONS WITH ANISOTROPIC DISTRIBUTIONS IN SOLAR FLARES. II. GYROSYNCHROTRON MICROWAVE EMISSION

Alexey A. Kuznetsov[1,2] and Valentina V. Zharkova[3]
[1] Armagh Observatory, Armagh BT61 9DG, UK
[2] Institute of Solar-Terrestrial Physics, Irkutsk 664033, Russia
[3] University of Bradford, Bradford BD7 1DP, UK
Received 2010 April 29; accepted 2010 August 11; published 2010 October 1

ABSTRACT

We investigate the spectra and polarization of the gyrosynchrotron microwave (MW) emission generated by anisotropic electron beams in the solar corona. The electron distributions are selected from the steady propagation/precipitation model of beam electrons obtained from the time-dependent solutions of the Fokker–Planck equation taking into account particle anisotropic precipitation into a converging magnetic tube while losing energy in collisions and Ohmic losses induced by a self-induced electric field. We separate the effects of converging magnetic field from those of self-induced electric field for beams with different initial energy fluxes and spectral indices. The effect of returning electrons of the beam is negligible for the beams with relatively weak energy fluxes ($F \lesssim 10^{10}$ erg cm^{-2} s^{-1}), while it becomes very important for the electron beams with $F \gtrsim 10^{12}$ erg cm^{-2} s^{-1}. Electric field-induced losses lead to the increase of MW emission intensity, especially at larger viewing angles ($\theta \gtrsim 140°$, looking at the loop from a side). The polarization remains typical for the beam-like distributions. The combined effect of the self-induced electric field and converging magnetic field reveals a noticeable (up to a factor of 10) increase of the emission intensity (for the viewing angles $\theta \simeq 140°$–$150°$) in comparison with the models considering only collision factor, especially in the deeper precipitation layers (near the loop footpoints). Thus, considering the self-induced electric field is especially important for the resulting MW emission intensity, spectra shape, and polarization that can provide much closer correlation of simulations with observations in solar flares.

Key words: Sun: flares – Sun: radio radiation

1. INTRODUCTION

Accelerated particles play a key role in the development of solar flares (e.g., Aschwanden 2005, and references therein). They are responsible for the energy transfer into flaring regions, for heating the chromospheric plasma as well as for producing radiation in a wide spectral range (from γ-rays to optical emission and radio waves) while some particles escape from the corona into the interplanetary space. Thus, investigation of high-energy particles is of primary importance for understanding the physics of solar flares and their influence on the near-Earth space.

The simultaneous observations of hard X-ray (HXR) and microwave (MW) emissions in footpoints of solar flares are often closely correlated in time pointing to their common origin (Aschwanden 2005; Bastian et al. 1998). There is a high likelihood of HXR and MW radiation being produced by the same population of non-thermal electrons (Kundu et al. 2001a, 2001b, 2004; Vilmer et al. 2002; Wilson & Holman 2003). Assuming that both kinds of emission are caused by the same population of electrons, the mechanisms of transport affecting the HXR and MW emission are substantially different: MW radiation is related to gyrosynchrotron emission of high-energy electrons with energies from few tens of keV (Kundu et al. 2001a) up to several MeV (Bastian 1999; Kundu et al. 2004), while HXR radiation is often produced by the electrons with much lower energies from 10 to 300 keV (see, for example, Lin et al. 2003; Holman et al. 2003).

At present, the HXRs and radio emission are considered to be the main diagnostic tools for the particles accelerated in the corona. These types of emission are produced by different mechanisms and usually in different parts of a flaring region. The HXRs, especially from harder beams, originate from the chromospheric sources where the particles lose their energy in the dense ambient plasma. On the other hand, the radio emission originates from the regions of a less dense plasma (where the plasma frequency does not exceed the emission frequency), that is, in the solar corona which also includes the particle acceleration sites. Thus, the X-rays and radio emission carry different (sometimes complementary) information about the parameters of the accelerated particles.

Despite significant progress in the theory of formation of gyrosynchrotron emission, the diagnostics of processes and conditions in the solar active regions by using the MW observations meets serious difficulties. This is caused by the fact that the MW emission characteristics depend on a number of parameters, such as plasma density, magnetic field strength, energy, and density of accelerated particles as well as the shape of electron distribution functions at different depths. At present, most studies use simplified expressions for the gyrosynchrotron emission parameters (e.g., Dulk & Marsh 1982). Those expressions were obtained for the case when the particles have isotropic (or, sometimes, weakly anisotropic) distribution on pitch angle and a simple (e.g., power law) distribution on energy.

However, existing models of particle acceleration and precipitation considering not only collisional but other energy-loss mechanisms unavoidably report anisotropic particle distributions which vary significantly with precipitation depth (for example, see distribution functions in Zharkova et al. 2010a, hereafter Paper I). Fleishman & Melnikov (2003a, 2003b) have shown that the pitch-angle anisotropy of accelerated particles, even if it is unable to support a coherent wave amplification, can change significantly the emission intensity (up to orders of magnitude) and polarization (the sign of circular polarization). Thus, the approximated electron distributions cannot be used in calculations of gyrosynchrotron emission. Instead, one has to consider, first, exact formulae for the MW emission which are rather cumbersome and computationally expensive, and second, to utilize more realistic distribution functions of accelerated electrons, which can account simultaneously for both HXR and MW emissions in solar flares.

A possible approach to solving this problem was given in the paper by Altyntsev et al. (2008), where the distribution of accelerated particles was described by the model function with two free parameters, which were chosen to provide the best fit to the observations. However, in reality, a reduction of the electron distribution function to a simple model carries out the essential model restrictions. In addition, in the paper by Altyntsev et al. (2008), the emission source was assumed to be homogeneous, meaning that variations of the parameters of the accelerated particles, plasma, and magnetic field along the magnetic loop were neglected.

The necessity to take into account the magnetic field convergence (which results in a formation of anisotropic distributions of the loss cone type) is commonly accepted. Nevertheless, only a few recent papers (e.g., Fleishman & Melnikov 2003a, 2003b; Altyntsev et al. 2008; Tzatzakis et al. 2008; Reznikova et al. 2009) really consider the effect of such distributions on the gyrosynchrotron radiation. In addition, spatial resolution of the existing MW instruments is not sufficient to obtain local values of the emission intensity and polarization, so all the parameters are being averaged over some area. However, this averaging of each parameter is strongly dependent on its depth variations as shown by Siversky & Zharkova (2009a). Therefore, one needs to apply a method that can determine electron distribution functions at different levels of a coronal magnetic loop (independently of MW observations), with a minimal number of the initial conditions.

This approach was developed in Paper I where the simulations were carried out for HXR emission and polarization from the power-law beam electrons precipitating into a flaring atmosphere from the corona. The electron distribution functions were obtained numerically by solving the time-dependent Fokker–Planck kinetic equation for the times of steady injection for collisional and Ohmic energy losses in converging magnetic loops. These energy-loss factors change the shape of electron distribution functions leading to some particles being reflected upward (the models for the calculation of distribution functions are described in detail in Paper I). The simulated distribution functions were already tested for the explanation of HXR emission, directivity, and polarization for many flaring events.

In this paper, we continue to investigate electron beam precipitation by extending the simulations to the radio emission produced by the same electron beams, namely, to the gyrosynchrotron emission in the MW range. Note that the emission in metric and decimetric ranges is also of great interest for diagnostics of the accelerated particles, acceleration mechanisms, and structure of the active regions. However, at these frequencies, the emission is caused mainly by different kinds of the coherent plasma mechanism (e.g., Dulk 1985, and references therein), which involves nonlinear processes and is not sufficiently developed yet (Aschwanden 2005). At the same time, MW emission is known to be mainly caused by incoherent radiation of accelerated electrons gyrating in the magnetic field; the theory of such a process is well developed and will be used in this paper.

Similar to Paper I, the electrons are assumed to be injected at the top of a magnetic loop and to propagate downward, toward the photosphere. Particle energy losses such as collisions with the ambient particles, anisotropic scattering, magnetic field inhomogeneity, and Ohmic losses in a self-induced electric field are considered. Then, we calculate (by using the exact expressions) the parameters of gyrosynchrotron emission from those particles, as for chosen levels of the coronal magnetic loop so for the loop as a whole (spatially integrated parameters). The model used is briefly described in Section 2. The results obtained for different depths and integrated ones are discussed in Sections 3 and 4, respectively. A comparison with the observations (for the 2002 July 23 flare) is carried out in Section 5. The conclusions are drawn in Section 6.

2. SIMULATION MODEL

Let us recapture some basic details of the electron precipitation model used in Paper I and to be used in this paper. The electrons are assumed to be injected at the top of the coronal magnetic loop as a directed collimated beam with power-law distribution over energy (E) and normal distribution over pitch-angle cosine (μ):

$$f(E,\mu)|_{z=0} \sim E^{-\gamma} \exp\left[-\frac{(\mu-1)^2}{\Delta\mu^2}\right], \quad (1)$$

for $E_{\min} < E < E_{\max}$, where the beam half-width in pitch angles $\Delta\mu \ll 1$. Further evolution of the electron beam during its steady precipitation into deeper atmospheric levels is described by the time-dependent Fokker–Planck equation (Paper I). We assume that ambient electrons are dragged into a reconnecting current sheet (RCS) formed by interacting magnetic loops and then steadily accelerated by a super-Dreicer electric field in the sheet (e.g., Litvinenko & Somov 1993; Zharkova & Agapitov 2009; Siversky & Zharkova 2009b). Such a process results in a steady ejection of electrons with power-law energy distribution from the current sheet into the loop. This electron beam injection is considered as the upper boundary condition in the current Fokker–Planck study of electron precipitation into the loop legs. It can be noted from our previous Fokker–Planck simulations (Siversky & Zharkova 2009a; Zharkova et al. 2010a) that a substantial part of those energetic electrons can return back to the acceleration site on the top (e.g., due to reflection from the magnetic mirror at the loop footpoint or to the effect of self-induced electric field) and join the ambient plasma electrons dragged into the RCS to be accelerated inside. Since the electric field accelerating the electrons toward a footpoint should decelerate the returning particles, the RCS region acts as a barrier preventing the particles from penetrating into the opposite half of the magnetic loop and bouncing between the footpoints.

This model allows us to consider only one-half of the magnetic loop between the acceleration site and a footpoint and to neglect completely the processes in the opposite half of the loop; the accelerated electrons in the opposite half of the loop can be produced by the same current sheet, but their properties and evolution should be considered separately since, technically, we have here two interlinked but different acceleration sites (Zharkova & Gordovskyy 2004; Siversky & Zharkova 2009b). The same electrons can make many journeys from the acceleration site to footpoint until either the reconnection process is seized or the injected electrons are fully thermalized in collisions at deeper layers. On the other hand, the returning electrons can alter the original electron distribution at the acceleration site as shown by Siversky & Zharkova (2009b), so the acceleration process itself becomes time dependent and the complete model of electron beam evolution has to include the processes in the acceleration site; however, this is out of scope of this paper.

Thus, we consider a quasi-stationary state when the beam injection rate is constant and the depth distributions of precipitating electrons after some timescale become well established and do not change in time. Such a state is usually achieved in about 70–200 ms after the injection onset (Siversky & Zharkova 2009a). Since we do not consider the particles bouncing between the loop footpoints and their accumulation inside the loop, this time would basically be the travel time of the particles from the top of the loop to the footpoint and back; higher energy electrons can return faster than lower energy ones unless they are thermalized by collisions. However, in the models including the self-induced electric field, some additional time is required to form a stationary return current compensating for the current of precipitating electrons (Siversky & Zharkova 2009a). Since the beams are assumed to have power-law energy distributions, the return current is mainly carried by low-energy electrons (tens of keV) whose density is highest and whose travel time defines the formation timescale of the quasi-stationary state. Note that due to the presence of electric field, this timescale is still much shorter than the collisional timescales.

The kinetic model (Fokker–Planck equation) takes into account the following factors of energy losses and direction changes.

1. Particle collisions (which result in electron loss of energy and change of pitch angle in every process of scattering).
2. Self-induced electric field (which results in a formation of the returning, or upward propagating, flow of particles reducing a return current of the ambient plasma).
3. Converging magnetic field (which reflects upward the particles with certain pitch angles).

We consider the models with pure collisions (C), collisions and electric field (CE), collisions and magnetic field convergence (CB), and with all the above losses (CEB) in order to investigate the relative contribution of the different processes to formation of the electron distributions and their resulting MW emission. In the simulations including the magnetic field convergence, the magnetic field (B) is assumed to increase exponentially with depth between the loop top and the characteristic depth in the transition region (Siversky & Zharkova 2009a). The background (thermal) plasma density (n_0) in the corona is assumed to be constant because the nearly barometric (exponential) height scale of the hot coronal plasma heated during the flares is expected to be very large—much greater than the typical loop height; the hydrodynamic simulations also show that plasma density in the corona is nearly constant or slowly increases with depth (Zharkova & Zharkov 2007).

In deeper layers (the transition region and chromosphere), magnetic field is constant in all models, and the plasma density increases rapidly with depth as per hydrodynamic models used and discussed in Paper I, thus providing fast precipitation of the injected electrons. While the kinetic model covers a large range of heights (from the loop top to the deep chromosphere), we consider the MW emission to be emitted only from the coronal part of the magnetic loop and assume that in deeper layers this emission cannot propagate due to a high plasma density. Instead of a linear distance z from the injection point, the Fokker–Planck equation is solved for a column density ξ, which is related to a linear distance z as $\xi = \int_0^z n(x)\,dx$, where n is the ambient plasma density; in the corona, we obtain $\xi \simeq zn_0$.

Table 1
Densities of the Precipitating Electrons (cm^{-3}) at the Injection Point for the Different Energy Fluxes and Power-law Indices of Electron Beams

F (erg cm^{-2} s^{-1})	$\gamma = 3$	$\gamma = 5$	$\gamma = 7$
10^{10}	2.2×10^7	5.0×10^7	6.0×10^7
10^{12}	2.2×10^9	5.0×10^9	6.0×10^9

In the simulations, we used the following parameters: the electron energy range 12 keV $< E <$ 1200 keV, the initial pitch angle half-width of an injected electron beam $\Delta\mu = 0.2$, and the magnetic field characteristic depth is located at $\xi_c = 10^{20}$ cm^{-2} (Siversky & Zharkova 2009a). The initial energy flux of energetic electrons F was taken to be 10^{10} and 10^{12} erg cm^{-2} s^{-1}, and the initial power-law index γ was taken to be 3 and 7 (the corresponding beam densities n_b on the upper boundary are given in Table 1). While the electron densities for $F = 10^{12}$ erg cm^{-2} s^{-1} seem very high (especially for the softer beams), we should note that this is caused mainly by the relatively small low-energy cutoff of the power-law distribution (12 keV) used in this work, so the total electron density is mainly the density of low-energy electrons which do not make a significant contribution into gyrosynchrotron radiation. Moreover, the numbers stated in Table 1 refer to the injection point, and the particle number decreases with the distance traveled (see, e.g., Zharkova & Kobylinskii 1993; Zharkova & Gordovskyy 2005). The magnetic convergence factor B_c/B_0 (the ratio of magnetic fields at the characteristic depth and the loop top) was equal to 1 (no convergence) and 3.

The examples of electron energy spectra at the column depth of 5×10^{19} cm^{-2} occurring between the injection point and the transition region are shown in Figure 1. Figures 1(a) and (b) demonstrate the effect of the electric field induced by beam electrons, which results in a formation of the returning electrons directed upward which reduce the return current formed by the ambient plasma electrons. For higher energy fluxes F of injected beams, this effect becomes stronger. The energy of the returning particles can reach $\sim$100 keV for $F = 10^{10}$ erg cm^{-2} s^{-1} and $\gtrsim$500 keV for $F = 10^{12}$ erg cm^{-2} s^{-1}. For $F = 10^{12}$ erg cm^{-2} s^{-1}, in a certain energy range, the number of electrons moving upward can even exceed the number of those electrons moving downward.

The effect of the converging magnetic field for beams with $F = 10^{12}$ erg cm^{-2} s^{-1} is demonstrated in Figure 1(c); for the beam with lower energy flux, the effect is very similar. One can see that the number of returning electrons is now smaller than in the model with the self-induced electric field. However, unlike the self-induced electric field, the converging magnetic field affects particles with all the energies. Thus, it forms the upward-directed flow of high-energy particles whose pitch angles exceed the loss-cone values and this effect is shown to be of a primary importance for the MW emission. The combined effect of the self-induced electric field and converging magnetic field results in a formation of the upward-directed electron flow (beam) with the whole spectrum of energies from low to high.

3. GYROSYNCHROTRON EMISSION FROM A HOMOGENEOUS SOURCE

Let us first recapture the variations of electron distribution functions in the Fokker–Planck approach and their effect on the MW emission. In order to do so (and also to compare our results with previous papers), we calculate the emission parameters under the assumption of a homogeneous source. In this case,

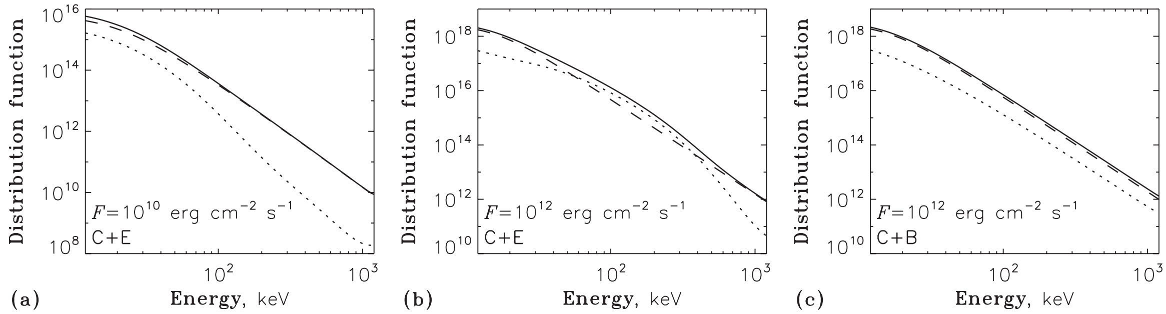

Figure 1. Electron distribution functions (integrated over pitch angles) obtained by solving the Fokker–Planck equation at the column depth $\xi = 5 \times 10^{19}$ cm^{-2}. Dashed line: electrons moving downward (with $\mu > 0$), dotted line: electrons moving upward (with $\mu < 0$), and solid line: the resulting distribution function (downward + upward). The initial power-law index of beam electrons is $\gamma = 3$, and the initial energy flux F is equal to 10^{10} or 10^{12} erg cm^{-2} s^{-1}. The factors taken into account are: collisions (C), self-induced electric field (E), and convergence of the magnetic field (B).

the equation of radiation transfer has a simple solution and the emission intensity (observed at the Earth) is equal to

$$I_\sigma = \frac{S}{\mathcal{R}^2} \frac{j_\sigma}{\varkappa_\sigma} (1 - e^{-\varkappa_\sigma L}) \tag{2}$$

for each magnetoionic mode σ. In the above expression, S is the visible source area, L is the source depth along the line of sight, and $\mathcal{R}$ is the astronomical unit. The formulae for the gyrosynchrotron plasma emissivity j_σ and absorption coefficient $\varkappa_\sigma$ are given in the Appendix. The polarization degree is defined as

$$\eta = \frac{I_X - I_O}{I_X + I_O}, \tag{3}$$

where I_O and I_X are the intensities of the ordinary and extraordinary modes, respectively.

In the present calculations, we used the following parameters: the visible source area $S = 1.8 \times 10^{18}$ cm^2, the source depth $L = 6 \times 10^8$ cm, the thermal plasma density $n_0 = 2 \times 10^9$ cm^{-3}, and the magnetic field strength at the considered depth $B = 370$ G. Note that in the models with converging magnetic field, the field strength must vary with depth, which is another factor (in addition to the variations of a distribution function) affecting the emission parameters. However, in this section, we assume that all the source parameters, except the electron distribution functions, remain the same in all calculations. A more complete simulation (including simultaneous variations of electron distributions and magnetic field) is performed in Section 4. The accepted magnitude of the thermal plasma density is relatively low and uncommon for the active regions of the solar corona. Moreover, this plasma density can be comparable to or even less than the particle density of the energetic electron component for very soft beams (see Table 1). However, our aim here is to rule out the Razin suppression and investigate the "pure" gyrosynchrotron radiation in the wide spectral range, including relatively low frequencies. The effect of higher plasma density is discussed in Section 3.4, where it is shown that all the conclusions made for the above-mentioned ambient density can be applied to a wider range of the coronal plasma densities.

The emission is characterized by its frequency ν and the angle θ between the wave vector and the magnetic field. We use the coordinate system where the angle $\theta = 0$ corresponds to the direction of the injected electron beam, i.e., toward the solar surface. Therefore, the observed at the Earth emission (if we neglect reflection and scattering) has to have $\theta > 90°$. We consider the cases of $\theta = 100°$ (almost transversal propagation that should be typical for limb flares) and $\theta = 140°$ (which, if we take into account the variety of shapes and tilts of the coronal magnetic loops, can take place in the flares located in various parts of the solar disk).

3.1. Effect of a Magnetic Field Convergence

The spectra and polarization of the emission produced by the different distributions of energetic particles (corresponding to the different heights) for initial energy flux $F = 10^{10}$ erg cm^{-2} s^{-1} and initial power-law index $\gamma = 3$ are shown in Figure 2(a) for the case when only collisions are taken into account while either the self-induced electric field or a convergence of magnetic field is neglected. One can see that both the emission spectra and polarization are almost the same for all the depths. For the viewing angle $\theta = 100°$, polarization is found to be very low. For $\theta = 140°$, in the optically thin part of the spectrum (where the emission intensity decreases with frequency), the X-mode dominates and polarization is positive.

By taking into account the magnetic field convergence in addition to collisions, the frequency distributions of MW intensity and polarization are changed dramatically (see Figure 2(b)). For $\theta = 100°$, the MW emission intensity (especially in the optically thin frequency range) increases with depth, and its spectral peak shifts toward higher frequencies. As a result, at the maximal depth considered in the model, the emission intensity exceeds by more than an order of magnitude the intensity for the pure collisional model. This is caused by the increase with depth of a number of particles having pitch angles around $\alpha \simeq 90°$. Near the injection point, polarization in the optically thin frequency range corresponds to the O-mode that is typical for a beam-like distribution (Fleishman & Melnikov 2003a; Fleishman & Kuznetsov 2010). In fact, we have here a two-stream distribution where both beams, the downward moving precipitating one and the upward moving returning one, are highly collimated. As the depth increases, the polarization is gradually dominated by the X-mode that is typical for loss-cone distributions.

The similar trend in polarization (contribution of X-mode increasing with depth) can be seen for the viewing angle $\theta = 140°$. However, in this case the emission intensity decreases with depth, due to a decrease of the number of particles having large pitch angles ($\alpha \gtrsim 140°$) while near the footpoint, the returning particles are mainly concentrated around 90°. Nevertheless, even at the deepest layer considered, the emission intensity is noticeably higher than for the pure collisional model meaning that there are more energetic electrons with the appropriate pitch angles in the emitting region in the corona.

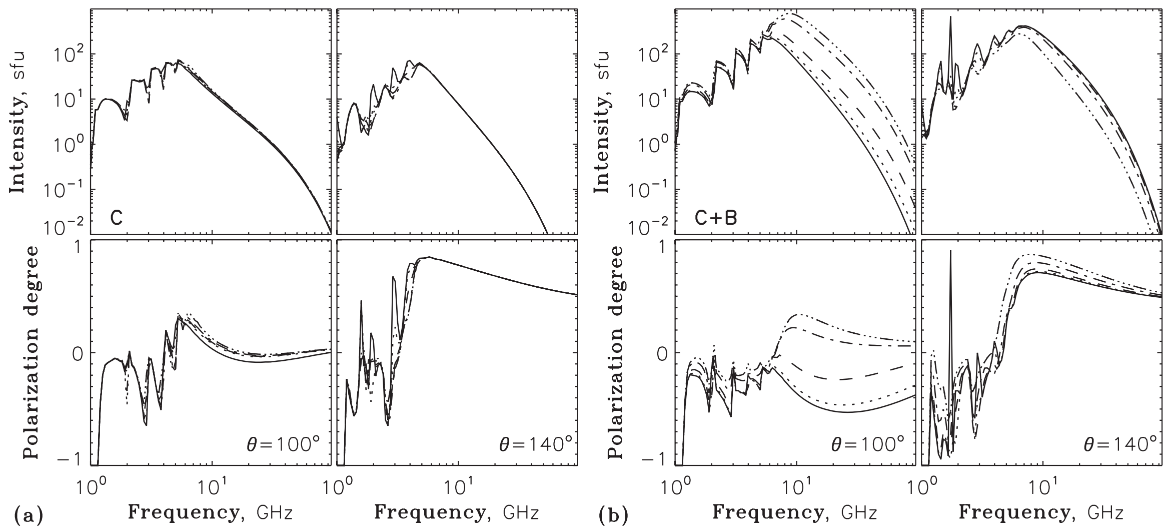

Figure 2. Intensity and polarization of the gyrosynchrotron emission from a homogeneous source (for different viewing angles). The used electron distribution functions are obtained by solving the Fokker–Planck equation with different factors taken into account (see Figure 1). The initial power-law index $\gamma = 3$, the initial energy flux $F = 10^{10}$ erg cm^{-2} s^{-1}, and other simulation parameters are given in the text. The different lines correspond to the electron distributions at different column depths from the injection point: solid line at $\xi = 2.4 \times 10^{17}$ cm^{-2}, dotted line at $\xi = 1.8 \times 10^{18}$ cm^{-2}, dashed line at $\xi = 5.5 \times 10^{18}$ cm^{-2}, dash-dotted line at $\xi = 1.6 \times 10^{19}$ cm^{-2}, and dash-triple-dotted line at $\xi = 5.0 \times 10^{19}$ cm^{-2}.

3.2. *Effects of a Self-induced Electric Field*

As we described in Paper I, the electric field induced by the precipitating beam is linearly dependent on the initial particle flux (and, therefore, their energy flux) on the top boundary and integrally on the electron distributions in energy and pitch angles at various depths which, obviously, will reflect various energy-loss mechanisms considered in the current study.

From electron distributions plotted in Figure 1, it can be noted that, for weaker electron beams with the energy flux $F = 10^{10}$ erg cm^{-2} s^{-1}, the effect of a self-induced electric field is relatively weak. As a result, for the weaker beams, inclusion of the self-induced electric field (in addition to collisions and the magnetic field convergence) does not much affect the emission spectra and polarization; they remain nearly the same as for pure collisions and collisions with converging magnetic field shown in Figures 2(a) and (b), respectively.

However, for a more intense hard electron beam, with the initial energy flux $F = 10^{12}$ erg cm^{-2} s^{-1} and the power-law index $\gamma = 3$, the emission spectra and polarization become significantly different (see Figure 3). At first, one can note that for the purely collisional model (Figure 3(a)) and for the model with collisions and converging magnetic field (Figure 3(b)), with the increase of the beam's initial energy flux, the MW emission intensities become higher by 2 orders of magnitude than for the beam with energy flux $F = 10^{10}$ erg cm^{-2} s^{-1}, and the spectral peaks are shifted toward higher frequencies. Depth variations of the emission parameters are qualitatively the same as for weaker beams (see Figures 2(a) and (b)).

When collisions and self-induced electric field are taken into account (see Figure 3(c)), the emission patterns are changed. We established earlier that the effect of the self-induced electric field becomes stronger with an increase of the energy flux F (see Figure 1) and spectral index (Zharkova & Gordovskyy 2006; Siversky & Zharkova 2009a). This effect is also observed in MW emission and polarization plotted in Figure 3(c). The self-induced electric field results in an immediate (just near the injection point) formation of a return current from the beam electrons scattered to pitch angles larger than 90°. This current is maintained for the whole time of the beam's steady precipitation, i.e., the particle distribution remains nearly unchanged with depth having two beams (precipitating and returning) traveling in the opposite directions. These two beams create a close electric circuit linking the injection site on the top with the whole loop where beam electrons precipitate.

Interesting effects come from looking at this emission from different viewing angles. For example, for the viewing angle $\theta = 100°$ (which is close to the transversal direction), the maximal intensity of MW emission is twice as high as for the purely collisional model. Furthermore, the spectral peaks keep being shifted further toward higher frequencies with depth, and the polarization in the optically thin part of the spectrum reveals a domination of the *O*-mode (beam-like distribution). For the viewing angle $\theta = 140°$ (looking at the loop from a side), the effect of the self-induced electric field becomes much stronger because the electrons of the return current are contributing more to the emission. It can be noted that the emission intensity is increased by a factor of about 5 while the polarization degree has decreased in comparison with the purely collisional model. This is because the returning electrons are shown in Paper I to have pitch angles between 90° and 180° with maximum close to the latter (Zharkova & Gordovskyy 2006) meaning that more emission is radiated to the oblique directions than to the transversal ones.

The electric field affects the MW emission and polarization calculated for the models including all three effects (collisions, self-induced electric field, and converging magnetic field) in a similar way, as shown in Figure 3(d). For the viewing angle $\theta = 100°$ (a limb flare), the effect of a self-induced electric field is relatively weak (in comparison with the effect of a converging magnetic field), so that both the spectra and polarization look similar to those in Figure 3(b), left panels. However, for the oblique viewing with $\theta = 140°$, the combined effect of the self-induced electric field and converging magnetic field results in a noticeable increase of the emission intensity (compare the right panels in Figures 3(b)–(d)). Also, note that the intensity of emission at $\theta = 140°$ almost does not decrease with depth now (contrary to what one can see in Figures 2(b) and 3(b)). This is

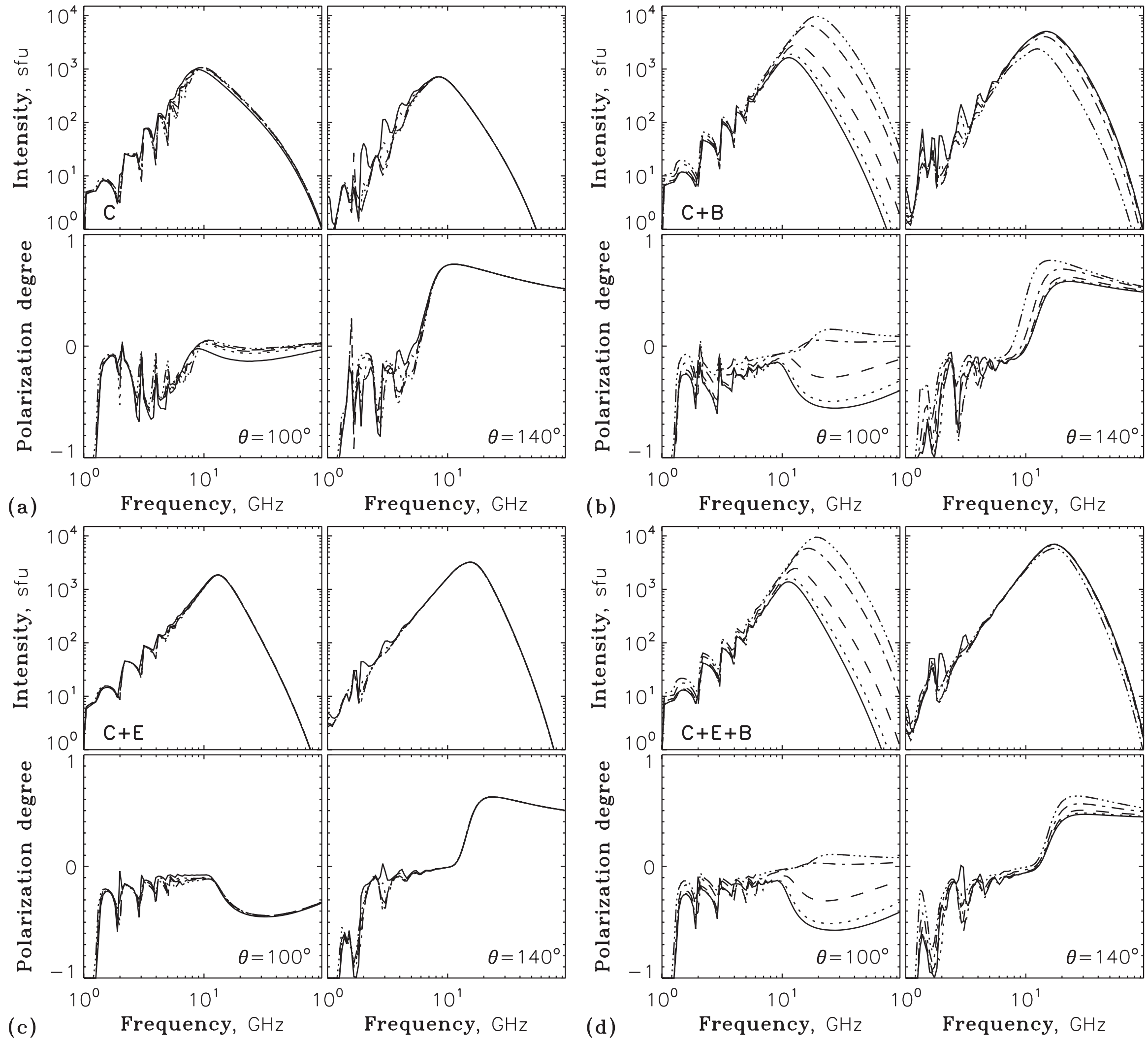

Figure 3. Same as in Figure 2, for $\gamma = 3$ and $F = 10^{12}$ erg cm^{-2}.

because the self-induced electric field drags the particles with pitch angles $\alpha \simeq 90°$ toward larger pitch angles. The importance of this effect is shown in Section 4.

3.3. *Effect of a Power-law Index of Beam Electrons*

Since the effects of electric field are more pronounced in HXR emission for softer beams (Zharkova & Gordovskyy 2006; Siversky & Zharkova 2009a; Zharkova et al. 2010a), let us compare the effect of a spectral index change of the intense electron beam on the MW emission and polarization. The simulation results for a softer electron beam with the initial power-law index $\gamma = 7$ (the energy flux $F = 10^{12}$ erg cm^{-2} s^{-1}) are plotted in Figure 4 which we compare with those for a hard beam plotted in Figure 3. For MW emission, the effect of electric field is more difficult to investigate because the increase of a power-law index results in a sharp decrease of the emission intensity and the shift of a spectral peak toward lower frequencies (where the spectrum is dominated by the harmonic structure).

Nevertheless, by comparing Figures 4(a) (purely collisional model) and (b) (with collisions and self-induced electric field), one can note that at larger depths the account for a self-induced electric field results in the well-noticeable increase of the emission intensity: by a factor of 2–3 for $\theta = 100°$ and by a factor of $\gtrsim$5 for $\theta = 140°$. That is, the relative effect of the self-induced electric field is nearly the same as for harder beams. A noticeable feature of the soft beams is that for $\gamma = 7$, the return current sets up slower than for $\gamma = 3$. In addition, the effect of collisions is more important now. The effect of a converging magnetic field for the beams with $\gamma = 7$ is qualitatively similar to that for beams with $\gamma = 3$ with a slight increase of the number of electrons mirrored by magnetic field back to the top for softer beams related to their faster collisional scattering to larger pitch angles above the loss cone.

3.4. *Effect of the Thermal Plasma Density*

The effect of the background (thermal) plasma on the gyrosynchrotron radiation has been investigated in many papers (e.g., Klein 1987; Fleishman & Melnikov 2003b; Melnikov et al. 2008). First of all, the emission cannot propagate if its frequency is below the cutoff frequency (which equals the electron plasma frequency for *O*-mode and is typically slightly higher for *X*-mode). In addition, the intensity of the gyrosynchrotron radiation decreases considerably (Razin 1960a, 1960b) if its frequency is below the Razin frequency $\nu_{\rm R} = 2\nu_{\rm p}/(3\nu_{\rm B})$, where $\nu_{\rm p}$ and $\nu_{\rm B}$ are the electron plasma and cyclotron frequencies. In the previous sections, we neglected the Razin suppression (by using a relatively low plasma density), in order to

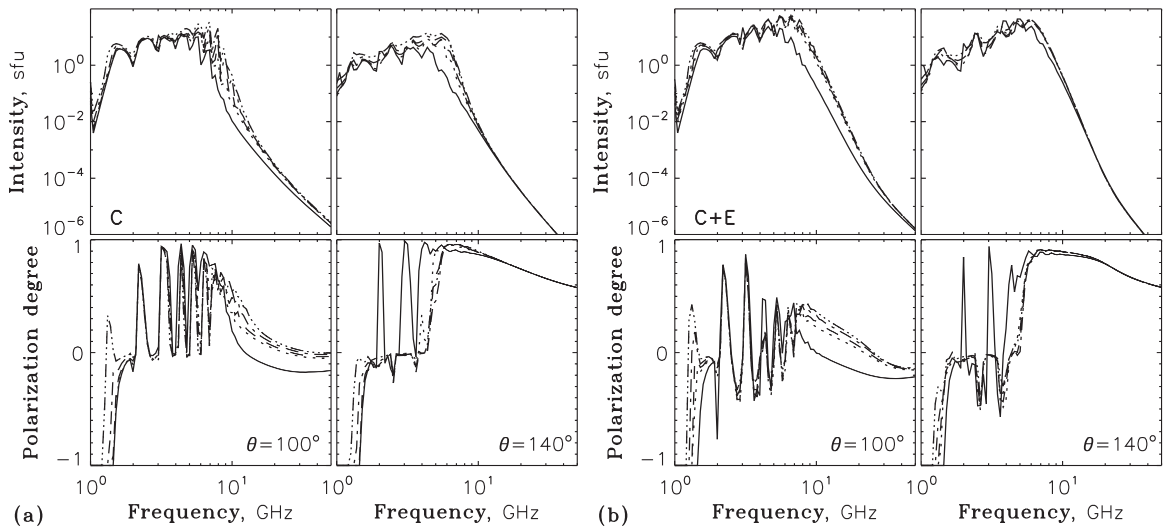

Figure 4. Same as in Figures 2 and 3, for $\gamma = 7$ and $F = 10^{12}$ erg cm^{-2}.

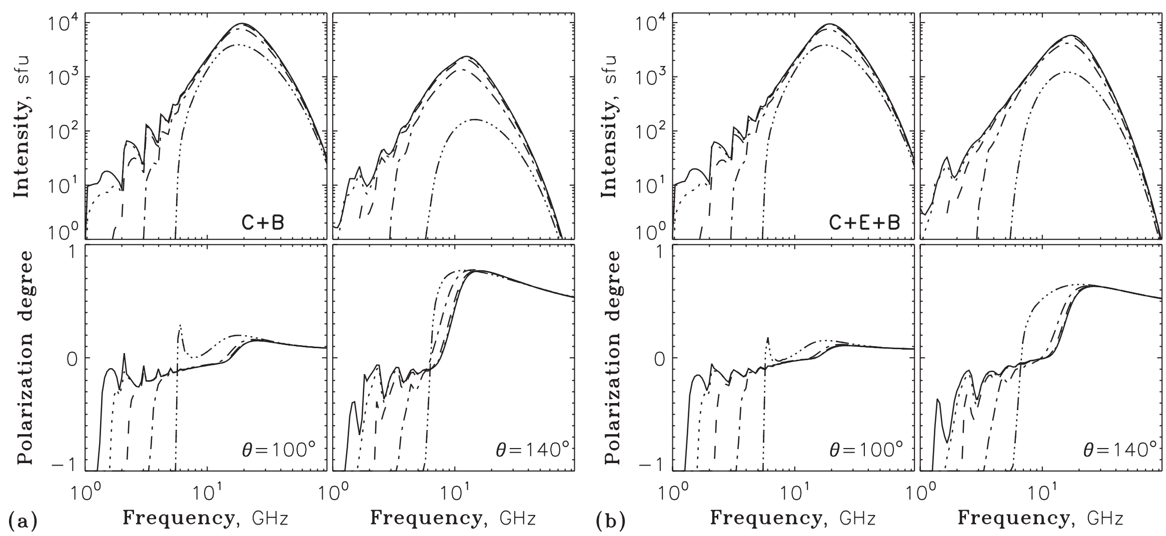

Figure 5. Spectra and polarization of the gyrosynchrotron emission from a homogeneous source (for two viewing angles: looking from upward at 100° and from a side at 140°). The different lines in each plot correspond to different magnitudes of the thermal plasma density n_0: solid line 3×10^9 cm^{-3}, dotted line 10^{10} cm^{-3}, dashed line 3×10^{10} cm^{-3}, dash-dotted line 10^{11} cm^{-3}, and dash-triple-dotted line 3×10^{11} cm^{-3}. The other simulation parameters and the distribution of energetic electrons are described in the text.

investigate in detail the effects of varying distributions of energetic electrons.

Figure 5 shows the emission spectra and polarization for five different values of the thermal plasma density (the magnetic field and source geometry are the same as in Figures 2–4). The initial parameters of the electron beam are: $F = 10^{12}$ erg cm^{-2} s^{-1}, $\gamma = 3$, and the plots in Figure 5 correspond to the distribution function at the depth equivalent to $\xi = 5.0 \times 10^{19}$ cm^{-2}. Two simulation models are considered (both including the collisions and converging magnetic field, but with or without self-induced electric field). One can see that the increasing plasma density makes the low-frequency (optically thick) slope of the spectrum more steep, and the low-frequency cutoff of the spectrum increases. On the other hand, the high-frequency (optically thin) part of the spectrum remains, in general, unaffected. The thermal plasma effects reach the optically thin range only for the highest considered plasma density (3×10^{11} cm^{-3}), when we have $\nu_R = 15.6$ GHz which is close to the spectral peak of the "pure" gyrosynchrotron emission. The emission spectra for other electron distributions (like those shown in Figures 2–4) will be affected by the increasing plasma density in a similar way.

Figures 5(a) and (b) also allow us to analyze the effect of self-induced electric field. The results are similar to those for the low-density plasma (see Figures 3(c) and (d)). We can see that for the viewing angle $\theta = 100°$ (nearly across the magnetic field), the self-induced electric field has almost no effect for all thermal plasma densities. On the other hand, for the oblique viewing angle $\theta = 140°$, inclusion of the self-induced electric field into the model results in a noticeable increase of the emission intensity. It is interesting to note that this effect becomes even stronger for the higher plasma densities: self-induced electric field increases the maximal emission intensity by an order of magnitude for $n_0 = 3 \times 10^{11}$ cm^{-3} and by a factor of about 3 for $n_0 = 10^{11}$ cm^{-3}, in contrast to the factor of about 2 for $n_0 = 3 \times 10^9$ cm^{-3}. Thus, we can conclude that, in spite of the fact that the variations of thermal plasma density can significantly affect the shape of gyrosynchrotron spectra at lower frequencies, the general effects of varying beam electron distributions (due to collisions, converging magnetic field, and

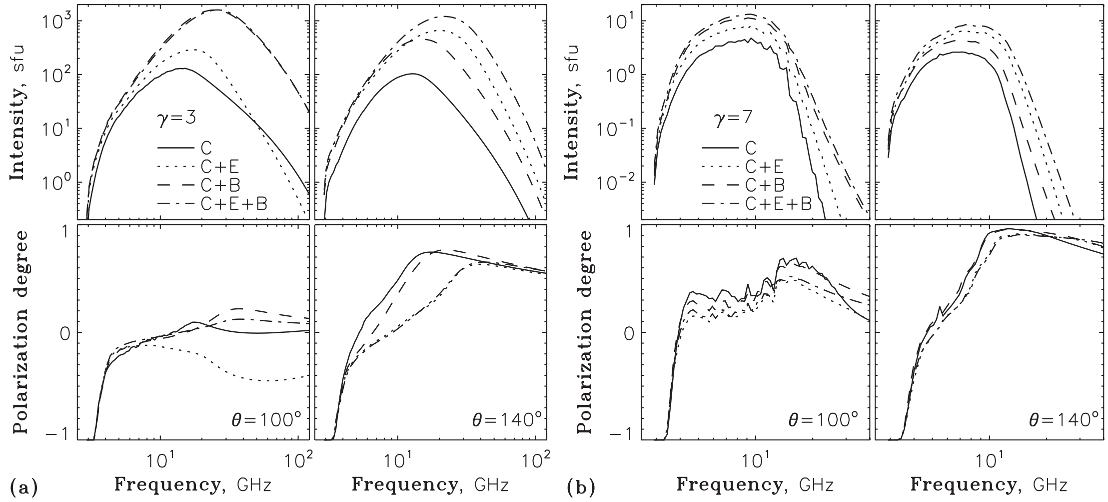

Figure 6. Intensity and polarization of the gyrosynchrotron emission from a whole coronal magnetic tube (for different viewing angles). The used electron distribution functions are obtained by solving the Fokker–Planck equation, and the adopted parameters and source geometry are given in the text. The different lines correspond to different simulation models (see Figure 1).

self-induced electric field) on those spectra remain rather similar for the ambient plasmas with different densities.

4. GYROSYNCHROTRON EMISSION FROM A WHOLE CORONAL MAGNETIC TUBE

Let us now investigate the MW emission from the whole coronal magnetic tube (spatially integrated in depth), as it is observed by the instruments without imaging capabilities.

As one can deduce from the previous section, variations of the electron distributions with precipitation depth noticeably affect the parameters of MW emission generated at different layers of a coronal magnetic tube. In addition, inhomogeneity of the magnetic field itself results in the significant variations of the emission parameters with height showing that with an increase of magnetic field magnitude, the emission intensity increases and the spectral peak shifts toward higher frequencies. As a result, the regions with strongest magnetic field (near the footpoints) make the dominant contribution into the MW emission of an active region, especially at high frequencies. The question is how the self-induced electric field will affect this MW emission and polarization.

We assume that all the parameters of the emission source depend only on the coordinate z, a linear distance along the magnetic tube related to the column density as described in Section 2. We also assume that the tube is relatively thin and the angle θ between the line of sight and the tube axis (magnetic field) does not differ much from 90°, so we can neglect variations of the source parameters along a single ray trajectory and consider the emission source as a superposition of separate quasi-homogeneous sources with the visible areas $dS = D(z)\,dz$, where $D(z)$ is the tube diameter at the height z. In this case, the total emission intensity can be estimated as

$$I_\sigma = \frac{1}{\mathcal{R}^2}\int\limits_{z_1}^{z_2} \frac{j_\sigma(z)}{\varkappa_\sigma(z)}[1 - e^{-\varkappa_\sigma(z)L(z)}]D(z)\,dz. \qquad (4)$$

Due to the requirement of the magnetic flux conservation, the tube diameter varies with depth as $D(z) = D(z_0)\sqrt{B(z_0)/B(z)}$ and the source depth at a given height can be estimated as $L(z) = D(z)/\sin\theta$. In the calculations, we used the following source parameters: tube diameter at the footpoint $D_0 =$ 5000 km, magnetic field at the footpoint $B_0 = 780$ G, distance between the electrons injection point, and the transition region z_c =10,000 km which corresponds to the thermal plasma density $n_0 = \xi_c/z_c = 10^{11}$ cm^{-3} (note that $n_b \ll n_0$ now).

In this section, we aim to investigate how the evolution of energetic particles distribution during their propagation affects the MW emission. This influence is expected to be qualitatively similar for all feasible source geometries. On this reason, possible variations of the parameters of plasma, magnetic field, and energetic particles across the magnetic tube in the above model are neglected. Also, the loop curvature is neglected as well, i.e., the viewing angle θ is assumed to be constant along the tube.

The spatially integrated emission spectra are shown in Figure 6 for the different simulation models (the initial energy fluxes of the energetic electrons $F = 10^{12}$ erg cm^{-2} s^{-1}, the initial power-law indices equal $\gamma = 3$ and 7). For the models C and C+E (pure collisions and collisions + self-induced electric field), the variation of magnetic field with depth is taken into account when calculating the emissivity and absorption coefficient while neglecting the effect of converging magnetic field on the distribution function.

Figure 6(a) shows the calculation results for a hard electron beam ($\gamma = 3$). First, we can note that for the viewing angle $\theta = 100°$, the main factor affecting the emission is the magnetic field convergence. The models with the converging magnetic field (C+B and C+E+B) provide much higher emission intensity than the models without this factor (C and C+E). The effect of the self-induced electric field is relatively weak and is visible only if we "turn off" the magnetic field convergence: the model with the return current (C+E) provides a higher peak intensity but a steeper intensity decrease with frequency than the purely collisional model (C); the difference of polarizations is noticeable as well. In the two models including the magnetic field convergence but either with (C+E+B) or without (C+B) self-induced electric field, the MW intensity and polarization are almost the same.

On the other hand, for $\theta = 140°$, the effect of the self-induced electric field exceeds that of the converging magnetic field: the model with collisions and self-induced electric field (C+E) provides a higher emission intensity than the model with collisions and magnetic field convergence (C+B). And the highest MW intensity is reached when taking into account the combined effect of a self-induced electric field and converging magnetic field in addition to collisions (C+E+B). Also, the self-induced electric field has a dominating effect on the emission polarization: we can see that the polarization plots are grouped in pairs according to whether the self-induced electric field is considered (C+E and C+E+B) or not (C and C+B).

The combined effect of a self-induced electric field and converging magnetic field turns the electrons moving upward to such pitch angles that their distribution maximum takes place at about $\mu = -0.8$ (Zharkova & Gordovskyy 2006) so that the direction where the particles emit the MW (and HXR) radiation corresponds to the intermediate viewing directions ($\theta \simeq 120^\circ$–150°). As a result, the account for the self-induced electric field (in the model C+E+B) results in the increase of the maximal intensity by a factor of about 3 (in comparison with the model C+B) and in a noticeable shift of the spectral peak from 15 to 23 GHz.

Figure 6(b) shows the calculation results for a softer electron beam ($\gamma = 7$). The emission intensity is now far less than for $\gamma = 3$. The effects of the converging magnetic field and self-induced electric field are qualitatively similar to those for harder beams. However, the relative differences between different models are now somewhat smaller—e.g., for the viewing angle $\theta = 140^\circ$, the maximal intensities for the C+B and C+E+B models differ by a factor of about 2. The polarization plots reveal very little difference between the different simulation models. All the above features are caused by the fact that the evolution of the soft electron beams during propagation is dominated by collisions, i.e., only a small fraction of the energetic particles can reach the loop footpoints (where the effects of particle anisotropy on the emission are the strongest). In addition, the stronger (in comparison to other factors) collisions produce more isotropic electron distributions than for harder beams. As a result, the relative importance of both the converging magnetic field and self-induced electric field (in comparison to collisions) decreases with an increase of the particle power-law index. Nevertheless, for the beams with $\gamma \simeq 7$, the effect of these factors on the MW emission intensity is noticeable and has to be considered when interpreting the observations.

The investigation presented here shows that the self-induced electric field and the part of a return current formed from the beam electrons themselves have to be considered when analyzing and interpreting MW observations. For relatively weak flares and the limb events, these factors are proved to be negligible. However, for more powerful flares (caused by electrons with higher electron fluxes and higher[4] spectral indices) located not very far from the disk center, the self-induced electric field is shown to produce the substantial effect on the emission intensity, spectrum shape, and polarization that can provide a much closer fit to the MW observations of a solar flare, like those presented in Zharkova et al. (2010b).

5. COMPARISON WITH OBSERVATIONS

In this section, we compare the predictions of our model with observations. We consider the flare of 2002 July 23. This X4.8 class flare was observed by many ground-based and space-borne instruments (see, e.g., Lin et al. 2003, and other articles published in the same journal issue). The Nobeyama Radio Polarimeter (NoRP; Nakajima et al. 1985) provided the spectra of the solar MW emission. Figure 7 shows a sample MW spectrum at the rise phase of the flare. The HXR observations (Holman et al. 2003) indicate that the energetic electrons at that time had the double power-law spectrum with the spectral indices of $\gamma_{\rm L} \simeq 4.5$–$5.5$ (below the break energy) and $\gamma_{\rm H} \simeq 6.5$–$7.5$ (above the break energy), and the energy flux $F \gtrsim 10^{12}$ erg cm^{-2} s^{-1}. The magnetograms reveal the presence of two spots (loop footpoints) with magnetic fields of about −650 G and +500 G (Zharkova et al. 2005) separated by a distance of about 10,000 km. The height of the magnetic loop can be estimated as 10,000–20,000 km, and the loop diameter near the footpoints was of the order of several thousand kilometers. The rise phase was chosen for analysis because at that time, as we expect, the emission was produced mainly by the precipitating and reflected energetic electrons, while at the latter phases of the flare the accumulated (near the top of the magnetic loop) electrons gave a significant contribution.

The loop occurred at the heliographical coordinates S13° E72°, so for the radial (perpendicular to the solar surface) magnetic field we obtain the angle between the magnetic field and line of sight of about 110°. However, the observations of γ-ray emission (Share et al. 2003) and HXR polarization (Emslie et al. 2008) suggest that there was a tilt of about 30°–40°, so the actual viewing angle with respect to the magnetic field was about 140°–150°. We consider here both cases of the loop orientation (with and without the tilt).

We use the source model similar to the one described in the previous section (a loop curvature is neglected). The emission is assumed to be a sum of the emissions from the two magnetic tubes with the footpoint magnetic fields of $B_1 = -650$ G and $B_2 = +500$ G, respectively. The footpoint tube diameters satisfy the relation $D_1/D_2 = \sqrt{|B_2/B_1|}$. The distance from the electron injection point to the transition region is taken to be z_c =20,000 km and the plasma density equals $n_0 = 5 \times 10^{10}$ cm^{-3} for both tubes. The energy flux of the accelerated electrons is $F = 10^{12}$ erg cm^{-2} s^{-1} and the power-law index $\gamma = 5$.

The theoretical curves in Figure 7(a) are calculated for the viewing angle $\theta = 110^\circ$ (i.e., without a tilt) and the tube diameters at the footpoints $D_1 = 6000$ km and $D_2 = 6850$ km. In Figure 7(b), we assume the tilt, so the viewing angle $\theta = 140^\circ$ and the tube diameters are taken to be $D_1 = 8000$ km and $D_2 = 9120$ km. We can see that the model used allows us to reproduce the maximal emission intensity and the spectral peak frequency. With decreasing frequency, the theoretical model predicts a faster decrease of the emission intensity than is really observed. This is because our model does not consider variations of the plasma density across the magnetic tube: as has been shown above, the emission frequency is limited from below by the local plasma frequency (which was equal to 2 GHz in our simulations); the Razin effect also suppresses the radiation at the low frequencies. In real magnetic loops, a decrease of the plasma density with distance from the loop axis (across the loop) will allow the MW emission to be generated at lower frequencies, so the spectrum will look like a superposition of different spectra (corresponding to the different plasma densities) in Figure 5. The simulation made by Melnikov et al. (2008) confirms that the account for the plasma inhomogeneity allows us to reproduce the observed MW spectra with a flat low-frequency slope.

The effect of the self-induced electric field is clearly seen for both viewing directions as plotted in Figures 7(a) and (b).

[4] For the same energy flux, the softer electron beams produce stronger X-ray emission since they release the bulk of their energy in the higher atmospheric layers, while the energy of harder beams goes mainly to plasma heating in the lower chromosphere (Zharkova & Gordovskyy 2006) thus producing weaker X-ray flares.

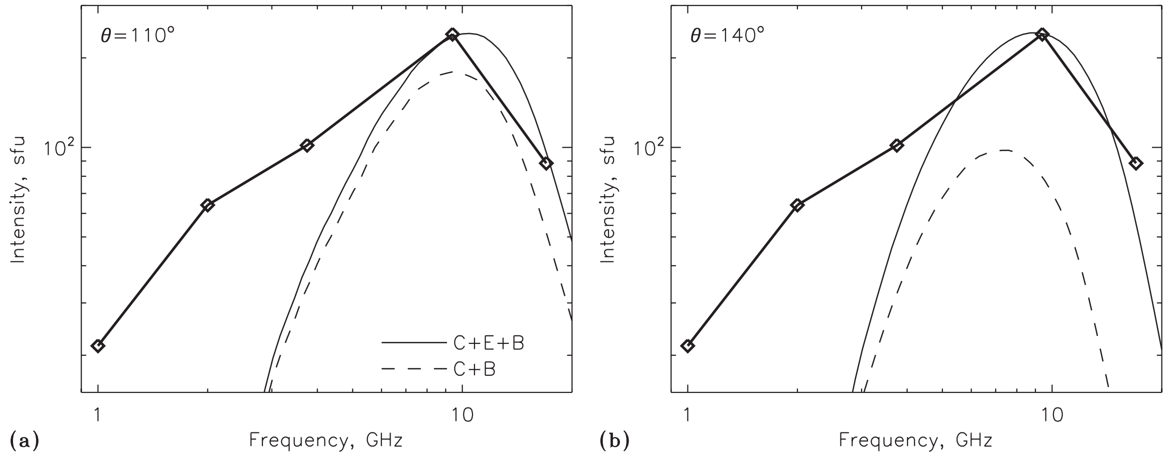

Figure 7. NoRP MW emission spectrum for the 2002 July 23 flare (at 00:26:00 UT), together with the theoretical predictions.

As we have shown in Section 3, the self-induced electric field (combined with the magnetic field convergence) increases the number of electrons moving upward with the intermediate pitch angles (between $\alpha = 90^\circ$ and $\alpha = 180^\circ$). In turn, this results in the increase of the MW emission intensity at the viewing directions $\theta \sim \alpha$. For the viewing angles close to $\theta = 90^\circ$, this effect is relatively weak (see Figure 7(a)). However, for the larger viewing angles (e.g., the case shown in Figure 7(b)), a neglect of the self-induced electric field decreases the calculated emission intensity by more than the factor of 2 (up to 10). Thus, the diagnostics of energetic particles based on the models without a self-induced electric field would overestimate by this factor the source size (or the abundance of energetic electrons).

The simulations carried out for both viewing angles can reasonably account for the MW observations of this flare. On the one hand, our simulations do not require a loop tilt in the 2002 July 23 event, on the other hand they also do not exclude it. However, for MW emission with the viewing angle $\theta = 110^\circ$, a smaller source size is required and the models with converging magnetic field with and without electric field give close results. At the same time, the model simulations of MW emission for $\theta = 140^\circ$ without electric field are much lower than those observed; the observations can be fit pretty closely only if the electric field is taken into account. Thus, the interpretation of the source properties based on MW observations only does not allow us to select the preferable viewing angle. This can be related mainly to the uncertainties of observations (such as the magnetic field measurements, loop size estimations, etc.) with some contribution related to a relative simplicity of the model.

6. CONCLUSION

In this paper, we investigated the energy spectra and polarization of the gyrosynchrotron MW emission generated by anisotropic electron beams in flaring atmospheres. The electron distributions are selected from the Fokker–Planck kinetic propagation/precipitation model, which takes into account energy losses and directivity change of beam electrons in collisions with the ambient particles, in converging magnetic field and a self-induced electric field.

The need to take into account magnetic field convergence which results in formation of anisotropic distributions of loss cone type is well accepted by many researchers while the effect of electric field was much more obscure. In this paper, for the first time, we explain the effects of a self-induced electric field as well as the combined effect of this electric field and converging magnetic field on MW emission parameters. We investigated the emission directed upward (to the observer at the Earth) that allowed us to establish the following.

1. The magnetic field convergence affects in a similar way the electron beams with different energy fluxes or power-law indices. The MW emission intensity for the viewing angles around $\theta \simeq 90^\circ$ increases with the increasing distance from the injection point of beam electrons, and for the larger viewing angles ($\theta \gtrsim 140^\circ$) it decreases. For $\theta \simeq 90^\circ$, the polarization sign reversal with depth is also observed exposing the increasing production of the *X*-mode.
2. The effect of returning electrons of the beam is negligible for the beams with relatively weak electron fluxes ($F \lesssim 10^{10}$ erg cm^{-2} s^{-1}), while it becomes very important for the electron beams with $F \gtrsim 10^{12}$ erg cm^{-2} s^{-1}.
3. Inclusion of the self-induced electric field effect into the simulation models (for electron energy fluxes $F \simeq 10^{12}$ erg cm^{-2} s^{-1}) results in the increase of MW emission intensity, especially, at large viewing angles ($\theta \gtrsim 140^\circ$). The polarization remains typical for the beam-like distributions.
4. The combined effect of the self-induced electric field and converging magnetic field reveals a noticeable (up to a factor of 10) increase of the emission intensity (for the viewing angles $\theta \simeq 140^\circ$–150°) in comparison with the models considering only collision factor, especially, in the deeper precipitation layers (near the loop footpoints). This is caused by the increased contribution of the emission of returning electrons—not only by those reflected by the converging magnetic field but also by those turned around by the self-induced electric field.
5. Thus, considering the self-induced electric field is especially important when interpreting the MW emission of powerful flares located close to the solar disk center. We found that including this factor into the simulation model (in addition to the magnetic field convergence and collisions) results in noticeable changes of the emission intensity, spectra shape, and polarization that can provide much closer fits to the MW observations of solar flares.

The authors thank the Royal Society (UK) for the visiting grant to the University of Bradford (2008 February) where the paper was initiated. A.A.K. thanks The Leverhulme Trust for financial support. V.V.Z. acknowledges the partial support of this work by the UK Science, Technology and Facility Council, grant PP-E001246, and the Royal Society Joint International grant (shared costs between the University of Bradford, UK and ISTP, Russia). This work was partially supported by the Russian Foundation for Basic Research, grants 08-02-92204 and 09-02-92610. The authors are very grateful to the respected referee for helpful comments and suggestions.

APPENDIX

GYROSYNCHROTRON PLASMA EMISSIVITY AND ABSORPTION COEFFICIENT

Exact equations for the gyrosynchrotron emissivity j_σ and absorption coefficient $\varkappa_\sigma$ have the form (Eidman 1958, 1959; Melrose 1968; Ramaty 1969)

$$j_\sigma = \frac{2\pi e^2}{c}\frac{N_\sigma \nu^2}{1+T_\sigma^2} \times \sum_{s=-\infty}^{\infty}\int\left[\frac{T_\sigma(\cos\theta - N_\sigma\beta\mu) + L_\sigma\sin\theta}{N_\sigma\beta\sin\theta\sqrt{1-\mu^2}}J_s(\lambda) + J_s'(\lambda)\right]^2 \times \beta^2(1-\mu^2)f(\mathbf{p})\delta\left[\nu(1-N_\sigma\beta\mu\cos\theta) - \frac{s\nu_B}{\Gamma}\right]d^3\mathbf{p}, \tag{A1}$$

$$\varkappa_\sigma = -\frac{2\pi e^2}{N_\sigma(1+T_\sigma^2)} \times \sum_{s=-\infty}^{\infty}\int\left[\frac{T_\sigma(\cos\theta - N_\sigma\beta\mu) + L_\sigma\sin\theta}{N_\sigma\beta\sin\theta\sqrt{1-\mu^2}}J_s(\lambda) + J_s'(\lambda)\right]^2 \times \beta(1-\mu^2)\left[\frac{\partial f(\mathbf{p})}{\partial p} + \frac{N_\sigma\beta\cos\theta - \mu}{p}\frac{\partial f(\mathbf{p})}{\partial\mu}\right] \times \delta\left[\nu(1-N_\sigma\beta\mu\cos\theta) - \frac{s\nu_B}{\Gamma}\right]d^3\mathbf{p}, \tag{A2}$$

where ν is the emission frequency, ν_B is the electron cyclotron frequency, N_σ, T_σ, and L_σ are the refraction index and the components of the polarization vector, respectively, θ is the angle between the wave vector and the magnetic field, p and β are the electron momentum and dimensionless speed, respectively, $\mu = \cos\alpha$, α is the electron pitch angle, $\Gamma = (1-\beta^2)^{-1/2}$ is the relativistic factor, $J_s(\lambda)$ and $J_s'(\lambda)$ are the Bessel function and its derivative over the argument λ,

$$\lambda = \frac{\nu}{\nu_B}\Gamma N_\sigma\beta\sin\theta\sqrt{1-\mu^2}. \tag{A3}$$

The electron distribution function $f(\mathbf{p})$ satisfies the normalization condition

$$\int f(\mathbf{p})\,d^3\mathbf{p} = n_{\mathrm{e}}, \tag{A4}$$

where n_{e} is the number density of energetic electrons.

Refraction index of the electromagnetic waves in plasma satisfies the dispersion equation

$$N_\sigma^2 = 1 - \frac{2V(1-V)}{2(1-V) - U\sin^2\theta + \sigma\sqrt{\mathcal{D}}}, \tag{A5}$$

where

$$\mathcal{D} = U^2\sin^4\theta + 4U(1-V)^2\cos^2\theta, \tag{A6}$$

$$U = \frac{\nu_B^2}{\nu^2}, \qquad V = \frac{\nu_p^2}{\nu^2}, \tag{A7}$$

and ν_p is the electron plasma (Langmuir) frequency. For the ordinary wave (O-mode), $\sigma = +1$; for the extraordinary wave (X-mode), $\sigma = -1$. The parameters T_σ and L_σ equal

$$T_\sigma = \frac{2\sqrt{U}(1-V)\cos\theta}{U\sin^2\theta - \sigma\sqrt{\mathcal{D}}}, \tag{A8}$$

$$L_\sigma = \frac{V\sqrt{U}\sin\theta + T_\sigma UV\sin\theta\cos\theta}{1-U-V+UV\cos^2\theta}. \tag{A9}$$

Equations (A1) and (A2) contain three-dimensional integrals over $d^3\mathbf{p}$. Using the properties of the δ-function, we can reduce those integrals to one-dimensional integrals over the parallel (to the magnetic field) component of the momentum vector p_z:

$$\left\{\begin{matrix} j_\sigma \\ \varkappa_\sigma \end{matrix}\right\} = \frac{4\pi^2 e^2}{c}\frac{N_\sigma\nu}{1+T_\sigma^2}\left\{\begin{matrix} 1 \\ -\frac{c}{N_\sigma^2\nu^2} \end{matrix}\right\} \times \sum_{s=1}^{\infty}\int_{p_{z\min}}^{p_{z\max}}\left[\frac{T_\sigma(\cos\theta - N_\sigma\beta\mu) + L_\sigma\sin\theta}{N_\sigma\beta\sin\theta\sqrt{1-\mu^2}}J_s(\lambda) + J_s'(\lambda)\right]^2 \times \left\{\begin{matrix} f(\mathbf{p}) \\ \frac{1}{\beta}\left[\frac{\partial f(\mathbf{p})}{\partial p} + \frac{N_\sigma\beta\cos\theta - \mu}{p}\frac{\partial f(\mathbf{p})}{\partial\mu}\right] \end{matrix}\right\} \times p^2(1-\mu^2)\,\mathrm{d}p_z\Bigg|_{p=p(p_z)}, \tag{A10}$$

where the momentum value $p(p_z)$ at every point of the resonance curve is found from the resonance condition:

$$p(p_z) = m_{\mathrm{e}}c\sqrt{\left(\frac{N_\sigma p_z\cos\theta}{m_{\mathrm{e}}c} + \frac{s\nu_B}{\nu}\right)^2 - 1}, \tag{A11}$$

$\mu(p_z) = p_z/p(p_z)$, and the integration limits $p_{z\min}$ and $p_{z\max}$ correspond to the boundaries of the interval where such a solution exists:

$$p_{z\min,\max} = m_{\mathrm{e}}c\frac{(s\nu_B/\nu)N_\sigma\cos\theta \mp \sqrt{N_\sigma^2\cos^2\theta + (s\nu_B/\nu)^2 - 1}}{1 - N_\sigma^2\cos^2\theta},$$

$$N_\sigma^2\cos^2\theta + \left(\frac{s\nu_B}{\nu}\right)^2 - 1 > 0. \tag{A12}$$

When obtaining Equation (A10), it is taken into account that for the electromagnetic waves (with $N_\sigma < 1$), the resonance condition can be satisfied only at $s \geqslant 1$. The gyrosynchrotron emissivity and absorption coefficient (A10) are calculated by numerical integration and consequent summation of the series over s. In this work, the integrals are evaluated using the Romberg method (Press et al. 1997). The series summation is stopped when a necessary accuracy (10^{-5}) is achieved. For the Bessel functions, we use the approximate formulae proposed by Wild & Hill (1971); the analysis made by Fleishman & Kuznetsov (2010) has shown that these formulae provide very high accuracy while reducing the computation time considerably in comparison with the exact Bessel functions.

The kinetic model (numerical solution of the Fokker–Planck equation) provides the electron distribution function as an array of values on a grid in (E, μ) space. Since the integration nodes in the numerical integration method, as a rule, do not coincide with the grid points, the resonance values of the distribution function and its derivatives were calculated using bilinear interpolation and the necessary transformations from (E, μ) space to (p, μ) space were applied.

REFERENCES

Altyntsev, A. T., Fleishman, G. D., Huang, G.-L., & Melnikov, V. F. 2008, ApJ, 677, 1367

Aschwanden, M. J. 2005, Physics of the Solar Corona (Chichester: Praxis)

Bastian, T. S. 1999, in Impulsive Flares: A Microwave Perspective, ed. T. S. Bastian, N. Gopalswamy, & K. Shibasaki, NRO Report No. 479, 211

Bastian, T. S., Benz, A. O., & Gary, D. E. 1998, ARA&A, 36, 131

Dulk, G. A. 1985, ARA&A, 23, 169

Dulk, G. A., & Marsh, K. A. 1982, ApJ, 259, 350

Eidman, V. Ya. 1958, Sov. Phys.—JETP, 7, 91

Eidman, V. Ya. 1959, Sov. Phys.—JETP, 9, 947

Emslie, A. G., Bradsher, H. L., & McConnell, M. L. 2008, ApJ, 674, 570

Fleishman, G. D., & Kuznetsov, A. A. 2010, ApJ, in press

Fleishman, G. D., & Melnikov, V. F. 2003a, ApJ, 584, 1071

Fleishman, G. D., & Melnikov, V. F. 2003b, ApJ, 587, 823

Holman, G. D., Sui, L., Schwartz, R. A., & Emslie, A. G. 2003, ApJ, 595, 97

Klein, K.-L. 1987, A&A, 183, 341

Kundu, M. R., Grechnev, V. V., Garaimov, V. I., & White, S. M. 2001a, ApJ, 563, 389

Kundu, M. R., Nindos, A., & Grechnev, V. V. 2004, A&A, 420, 351

Kundu, M. R., Nindos, A., White, S. M., & Grechnev, V. V. 2001b, ApJ, 557, 880

Lin, R., et al. 2003, ApJ, 595, 69

Litvinenko, Yu. E., & Somov, B. V. 1993, Sol. Phys., 146, 127

Melnikov, V. F., Gary, D. E., & Nita, G. M. 2008, Sol. Phys., 253, 43

Melrose, D. B. 1968, Ap&SS, 2, 171

Nakajima, H., Sekiguchi, H., Sawa, M., Kai, K., Kawashima, S., & Shiomi, Y. 1985, PASJ, 37, 163

Press, W. H., Teukolsky, S. A., Vetterling, W. T., & Flannery, B. P. 1997, Numerical Recipes in C: The Art of Scientific Computing (2nd ed.; Cambridge: Cambridge Univ. Press)

Ramaty, R. 1969, ApJ, 158, 753

Razin, V. A. 1960a, Izv. Vyssh. Uchebn. Zaved. Radiofiz., 3, 584

Razin, V. A. 1960b, Izv. Vyssh. Uchebn. Zaved. Radiofiz., 3, 921

Reznikova, V. E., Melnikov, V. F., Shibasaki, K., Gorbikov, S. P., Pyatakov, N. P., Myagkova, I. N., & Ji, H. 2009, ApJ, 697, 735

Share, G. H., et al. 2003, ApJ, 595, 89

Siversky, T. V., & Zharkova, V. V. 2009a, A&A, 504, 1057

Siversky, T. V., & Zharkova, V. V. 2009b, J. Plasma Phys., 75, 619

Tzatzakis, V., Nindos, A., & Alissandrakis, C. E. 2008, Sol. Phys., 253, 79

Vilmer, N., Krucker, S., Lin, R. P., & The RHESSI Team. 2002, Sol. Phys., 210, 261

Wild, J. P., & Hill, E. R. 1971, Aust. J. Phys., 24, 43

Wilson, R. F., & Holman, G. D. 2003, AAS SPD Meeting, 34, 1620

Zharkova, V. V., & Agapitov, O. 2009, J. Plasma Phys., 75, 151

Zharkova, V. V., & Gordovskyy, M. 2004, ApJ, 604, 884

Zharkova, V. V., & Gordovskyy, M. 2005, A&A, 432, 1033

Zharkova, V. V., & Gordovskyy, M. 2006, ApJ, 651, 553

Zharkova, V. V., & Kobylinskii, V. A. 1993, Sol. Phys., 143, 259

Zharkova, V. V., Kuznetsov, A. A., & Siversky, T. V. 2010a, A&A, 512, A8

Zharkova, V. V., Meshalkina, N. S., Kashapova, L. K., Kuznetsov, A. A., Altyntsev, A. T., & Grechnev, V. V. 2010b, A&A, submitted

Zharkova, V. V., & Zharkov, S. I. 2007, ApJ, 664, 573

Zharkova, V. V., Zharkov, S. I., Ipson, S. S., & Benkhalil, A. K. 2005, J. Geophys. Res., 110, A08104